PHOTONICS Research

Tunable terahertz wave difference frequency generation in a graphene/AlGaAs surface plasmon waveguide

Tao Chen,[1,*] Liangling Wang,[1] Lijuan Chen,[1] Jing Wang,[1] Haikun Zhang,[1] and Wei Xia[1,2]

[1]School of Physics and Technology, University of Jinan, Jinan 250022, China
[2]e-mail: sps_xiaw@ujn.edu.cn
*Corresponding author: taochen426@hust.edu.cn

Received 14 November 2017; revised 18 January 2018; accepted 18 January 2018; posted 19 January 2018 (Doc. ID 313519); published 27 February 2018

Graphene-based surface plasmon waveguides (SPWs) show high confinement well beyond the diffraction limit at terahertz frequencies. By combining a graphene SPW and nonlinear material, we propose a novel graphene/AlGaAs SPW structure for terahertz wave difference frequency generation (DFG) under near-infrared pumps. The composite waveguide, which supports single-mode operation at terahertz frequencies and guides two pumps by a high-index-contrast AlGaAs/AlO_x structure, can confine terahertz waves tightly and realize good mode field overlap of three waves. The phase-matching condition is satisfied via artificial birefringence in an AlGaAs/AlO_x waveguide together with the tunability of graphene, and the phase-matching terahertz wave frequency varies from 4 to 7 THz when the Fermi energy level of graphene changes from 0.848 to 2.456 eV. Based on the coupled-mode theory, we investigate the power-normalized conversion efficiency for the tunable terahertz wave DFG process by using the finite difference method under continuous wave pumps, where the tunable bandwidth can reach 2 THz with considerable conversion efficiency. To exploit the high peak powers of pulses, we also discuss optical pulse evolutions for pulse-pumped terahertz wave DFG processes.

OCIS codes: (190.4223) Nonlinear wave mixing; (240.6680) Surface plasmons; (230.7370) Waveguides; (160.6000) Semiconductor materials.

https://doi.org/10.1364/PRJ.6.000186

1. INTRODUCTION

Graphene has recently attracted huge interest in the optoelectronics field [1], such as passively mode-locked lasers [2,3], broadband polarizers [4], chemical gas sensing [5], optical modulators or switches [6,7], photodetectors [8], enhanced four-wave mixing [9], terahertz (THz) and infrared spectroscopy [10], and plasmonics [11,12]. Graphene-based plasmons enable strong confinement of the optical field at subwavelength scales and hold great potential for applications [13], which can be tuned via gate bias voltage, chemical doping, the electric field, or the magnetic field [14]. To guide graphene surface plasmons with deep subwavelengths, many types of graphene surface plasmon waveguides (GSPWs) have been proposed [4,6,9,15,16]. At THz frequencies, the tunability, excitation, and generation of graphene surface plasmons have been demonstrated [17–19]. Liu *et al.* investigated the effective refractive index, loss, and effective mode area of a 100 μm width Si–SiO_2–graphene–dielectrics–graphene–SiO_2–Si waveguide for different Fermi energy levels (chemical potentials) [20], where the loss and effective index can be reduced with increasing Fermi energy level when the resultant optical mode area increases. Zhou *et al.* proposed a hybrid few-layer GSPW to balance the loss and mode area through the strong coupling between the dielectric waveguide and plasmon waveguide [21]. Furthermore, Xu *et al.* analyzed the single-mode operation region of a dielectric-loaded GSPW with different Fermi energy levels [22]; the optical properties of the fundamental mode can be tuned by changing the Fermi energy level, and the waveguide is simple and easy for fabrication.

THz sources are important for many applications of THz waves [23]. The four-wave mixing (FWM) and difference frequency generation (DFG) in waveguide devices are important techniques to generate coherent THz waves through nonlinear wavelength conversion. Barh *et al.* reported an all-fiber FWM THz source in a microstructured-core double-clad plastic fiber pumped by a high-power CO_2 laser [24]. Sun *et al.* proposed a hybrid graphene sheets waveguide for THz FWM generation [25], where the waveguide supports graphene surface plasmon modes at THz frequencies. Compared with the FWM process, the DFG technique is more attractive because of its high

quadratic nonlinearity, which has been investigated in many conventional waveguides, such as the $LiNbO_3$ ribbon waveguide [26], the periodically poled $LiNbO_3$ rectangular waveguide [27], the THz surface-emitted GaAs/AlAs modal birefringence waveguide [28], and the $Al_xGa_{1-x}As$ nested waveguide heterostructure [29]. Due to the large wavelength difference between the optical pump and THz waves, the THz conventional waveguides have a dimension of hundreds of microns, so the mode field overlaps are unsatisfactory. To confine THz more tightly, we proposed an AlGaAs photonic crystal waveguide with the scales of tens of microns to achieve THz generation [30]. Ruan *et al.* analyzed the THz DFG from a micron-scale GaAs strip, which is embedded within a metallic slot waveguide [31], but the THz mode field concentrates in the metallic region and leads to a reduced mode field overlap. Ge *et al.* investigated a gold nanowire array on the surface of lithium niobite crystal for guiding both optical and terahertz waves by surface plasmonic modes with a rather small mode overlapping area [32], and the THz waves can be surface-emitted based on the Čherenkov phase-matched DFG process with 4 μm propagation length, which is smaller than the coherence length. On the other hand, the conversion bandwidth of the THz DFG process is quite narrow in conventional waveguides because of the strict phase-matching condition.

To exploit the valuable deep-subwavelength confinement and tunability of the THz GSPW, in this paper we analyze in detail the use of a graphene/AlGaAs surface plasmon waveguide for colinear and tunable THz wave DFG under near-infrared pumps. At THz frequencies, the waveguide provides single-mode surface plasmon confinement with highly effective refractive indices, and the mode field overlap between pump and THz waves is greatly improved. The phase-matching condition is achieved by adjusting the Fermi energy level of graphene and employing the artificial birefringence at near-infrared frequencies in high-index-contrast AlGaAs/AlO_x waveguides. We mainly focus on THz wave generation with a 6 THz central frequency; tunable THz wave generation from 4 to 7 THz is realized through changing the signal wavelength and adjusting the Fermi energy level of graphene from 0.848 to 2.456 eV. Based on coupled-mode theory, we investigate the conversion efficiency and pulse evolutions of tunable THz wave DFG processes by using the finite difference method under continuous wave (CW) and pulse pumps, respectively. Such a tunable THz source, which can allow larger manufacturing tolerances, may be easy to integrate with other THz GSPW structures for applications.

2. WAVEGUIDE STRUCTURE AND THEORETICAL MODEL

The waveguide structure, as shown in Fig. 1, consists of a nonlinear $Al_{0.5}Ga_{0.5}As$ strip embedded in an AlO_x-loaded GSPW. The $Al_{0.5}Ga_{0.5}As$ core layer is chosen to avoid two-photon absorption and for its easy fabrication process [33,34]. Owing to a negligible difference of refractive indices between $Al_{0.5}Ga_{0.5}As$ and AlO_x at THz frequencies [35], the mode field will concentrate in the central $Al_{0.5}Ga_{0.5}As$ region. The high-index-contrast AlGaAs/AlO_x structure is designed to provide strong mode field confinement and birefringence between TE and

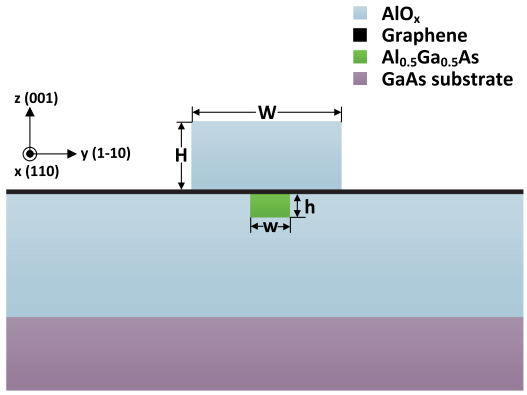

Fig. 1. Schematic of the graphene/AlGaAs surface plasmon waveguide.

TM modes for two pumps, which is important for good mode field overlap and the phase-matching condition. W, H, w, and h are the width and height of AlO_x and $Al_{0.5}Ga_{0.5}As$ strips, respectively. The structure may grow on GaAs substrates [(001) crystal direction] by using standard semiconductor growth and processing techniques [e.g., molecular beam epitaxy or plasma-enhanced chemical vapor deposition (PECVD)] [36], where $Al_{0.93}Ga_{0.07}As$ is used for the lower cladding layer. Photolithography, regrows $Al_{0.5}Ga_{0.5}As$ and $Al_{0.93}Ga_{0.07}As$ to obtain the lower waveguide structure, and then thermally oxidation converts the $Al_{0.93}Ga_{0.07}As$ lower cladding layers to AlO_x layers [37]. The monolayer graphene may be fabricated by high-quality CVD, which grows on the polished lower waveguide structure [38], and the upper AlO_x strip may be formed by the atomic layer deposition technique [6,39].

The model considers the THz DFG process, and the propagation direction is along the x axis [(110) crystal direction], as shown in Fig. 1. Under the slowly varying envelope approximation, where the electric field amplitude changes slowly relative to the fast optical carrier frequency, we can derive the following coupled-mode equations for the DFG process [40]:

$$\begin{aligned}
&\frac{\partial A_p}{\partial x}+\beta_p^1\frac{\partial A_p}{\partial t}+\frac{1}{2}\alpha_p A_p = i\omega_p\kappa A_s A_i\ \exp(-i\Delta kx),\\
&\frac{\partial A_s}{\partial x}+\beta_s^1\frac{\partial A_s}{\partial t}+\frac{1}{2}\alpha_s A_s = i\omega_s\kappa A_i^* A_p\ \exp(i\Delta kx),\\
&\frac{\partial A_i}{\partial x}+\beta_i^1\frac{\partial A_i}{\partial t}+\frac{1}{2}\alpha_i A_i = i\omega_i\kappa A_s^* A_p\ \exp(i\Delta kx),
\end{aligned}\tag{1}$$

where $A_{p,s,i}$ are the normalized complex amplitudes of the pump, signal, and THz waves, respectively, which are as functions of the position x and time t. $|A_{p,s,i}|^2 = P_{p,s,i}$ denote the powers. $\beta^1_{p,s,i}$ stand for the reciprocal value of group velocity, and $\alpha_{p,s,i}$ are the propagation loss coefficients. $\omega_{p,s,i}$ are the angular frequencies, and $\omega_i = \omega_p - \omega_s$ satisfies energy conservation. $\Delta k = k_p - k_s - k_i$ expresses the phase mismatch, and $k_{p,s,i}$ are the corresponding wavevectors for $\omega_{p,s,i}$. The parameter κ refers to the DFG coupling coefficient,

$$\kappa = d_{\text{eff}}\sqrt{2\mu_0/(cn_p n_s n_i A_{\text{eff}})},\tag{2}$$

where d_{eff} is the effective nonlinear coefficient. For the DFG process in the GSPW of Fig. 1, the TE pump (ω_p) and TM signal (ω_s) generate TM THz wave (ω_i). Thus, $d_{\text{eff}} = d_{14} = 47$ pm/V, where d_{14} is the AlGaAs nonlinear coefficient [29]. $n_{p,s,i}$ are the effective refractive indices. A_{eff} is the effective nonlinear interaction area and can be expressed as

$$A_{\text{eff}} = \frac{\iint |e_p|^2 \mathrm{d}y\mathrm{d}z \iint |e_s|^2 \mathrm{d}y\mathrm{d}z \iint |e_i|^2 \mathrm{d}y\mathrm{d}z}{|\iint e_p e_s e_i \mathrm{d}y\mathrm{d}z|^2}, \tag{3}$$

where $e_{p,s,i}$ are the transverse mode field profiles.

A. Field Distribution

The relative permittivity of graphene is equivalently expressed as $\varepsilon_g = 1 + \frac{i\delta_g}{\omega\varepsilon_0\Delta}$, and monolayer graphene can be treated as an ultrathin film layer with a thickness of $\Delta = 0.5$ nm [14]. ω is the angular frequency of optical waves. δ_g is the optical surface conductivity of graphene, which is related to temperature T, angular frequency ω, Fermi energy level E_F, and momentum relaxation time τ [41]. We have

$$\delta_g = i\frac{e^2 k_B T}{\pi\hbar^2(\omega + i\tau^{-1})}\left\{\frac{E_F}{k_B T} + 2\ln\left[\exp\left(-\frac{E_F}{k_B T}\right) + 1\right]\right\} + i\frac{e^2}{4\pi\hbar}\ln\left[\frac{2|E_F| - \hbar(\omega + i\tau^{-1})}{2|E_F| + \hbar(\omega + i\tau^{-1})}\right], \tag{4}$$

where k_B is the Boltzmann constant, and $T = 300$ K at room temperature. Relaxation time $\tau = \mu E_F/(ev_F^2)$ is determined by the carrier mobility μ, Fermi velocity v_F, and Fermi energy level E_F. The parameters μ and v_F are considered to be $10,000\ \text{cm}^2/(\text{V}\cdot\text{s})$ and 10^6 m/s, respectively [22].

The refractive index of graphene is $\sqrt{\varepsilon_g} = n + ik$, where n and k correspond to the real and imaginary parts of the refractive index, as shown in Figs. 2(a) and 2(b), respectively. n and k both decrease with increasing THz wave frequency when k increases with the increasing E_F. We calculate the effective refractive indices and mode field distribution of three waves by the finite-element-method-based commercial COMSOL mode solver. We analyze the complex effective index n_{eff} for single-mode THz GSPW under different values of n and k. The real part of n_{eff} is n_i in Eq. (4), and the imaginary part of n_{eff} indicates the loss as $\alpha_i = 4\pi\,\text{Im}(n_{\text{eff}})/\lambda_i$ in Eq. (1). W and H in Fig. 1 are adjusted to realize the single-mode operation. It is found that n affects the loss α_i and k relates to the mode field confine, respectively. When E_F increases, the smaller n brings about lower loss and the bigger k requires larger dimension W and H for single-mode operation. Therefore, there is a tradeoff between loss and mode field confinement. That is, while the loss is reduced, the single-mode structure will result in a large mode field area. It is worth noting that we also investigate the influence of few-layer graphene (e.g., two layers) on the THz GSPW, where the few-layer graphene just reduces E_F for the single-mode condition with fixed W and H, but the loss cannot be reduced.

Figures 3(a)–3(c) show the electric field of the TM single mode for 6 THz and fundamental modes for $\lambda_p = 1.53$ μm and $\lambda_s = 1.5783$ μm under the phase-matching condition, which will be discussed in the following. From Fig. 3(a), the waveguide confines the THz mode field very tightly and

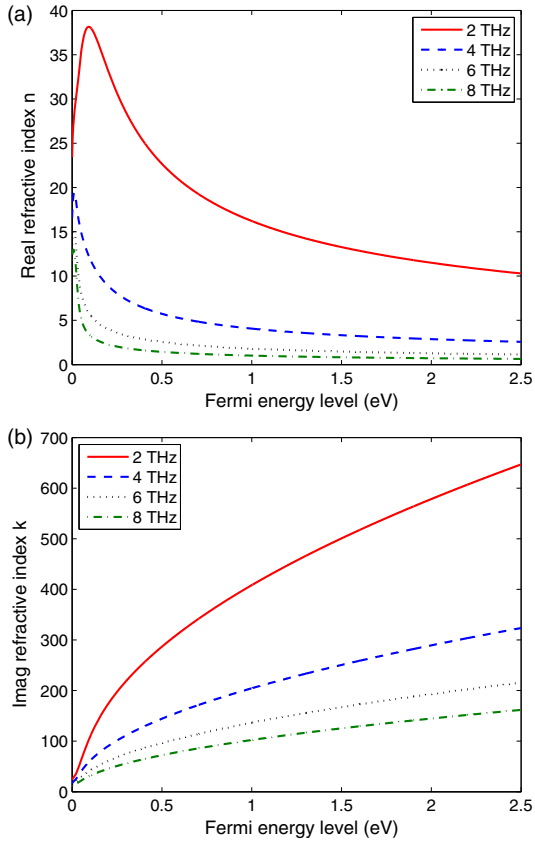

Fig. 2. (a) Real and (b) imaginary refractive index of graphene versus the Fermi energy level for 2, 4, 6, and 8 THz, respectively.

the electric field is restricted around the AlGaAs dielectric. In vertical direction, it is continuous for the electric field of TE λ_p, as shown in Fig. 3(b), or for the electric displacement field of TM λ_s, as shown in Fig. 3(c). Calculating the overlap integral of Eq. (3), we obtain the effective nonlinear interaction

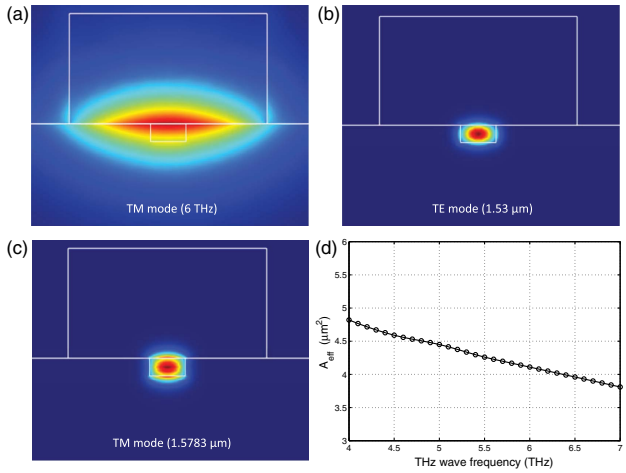

Fig. 3. Electric field profiles of (a) TM single mode at 6 THz, (b) TE fundamental mode at pump wavelength $\lambda_p = 1.53$ μm, and (c) TM fundamental mode at signal wavelength $\lambda_s = 1.5783$ μm. (d) Effective interaction area A_{eff} as a function of THz wave frequency.

area A_{eff} for different phase-matching THz wave frequencies, as shown in Fig. 3(d). A_{eff} is around 4 μm^2, which is small enough compared with the large THz wavelength. Although A_{eff} can be decreased through reducing the dimension of waveguide structure and tuning E_F of graphene, the loss will increase sharply.

B. Phase-Matching Analysis

The phase-matching condition is $\Delta k = k_p - k_s - k_i = 0$, where $k_{p,s,i} = 2\pi n_{p,s,i}/\lambda_{p,s,i}$, and $\lambda_{p,s,i} = c/\omega_{p,s,i}$ are the vacuum wavelengths of three waves. Due to the high THz effective refractive index n_i of GSPW, we employ the birefringence of the high-index-contrast AlGaAs/AlO_x structure to realize the phase matching. Based on $\omega_i = \omega_p - \omega_s$ and the phase-matching condition, the difference of effective refractive indices between pump and signal can be expressed as

$$n_p - n_s = \frac{\omega_i}{\omega_p}(n_i - n_s). \tag{5}$$

The dielectric constant of nonlinear $Al_xGa_{1-x}As$ material can be accurately derived from the formula $\varepsilon(Al_xGa_{1-x}As) = x\varepsilon(AlAs) + (1-x)\varepsilon(GaAs)$ [35]. The material absorption factors are associated with the imaginary parts of the refractive index. There are not strict formulas for AlO_x and $Al_xGa_{1-x}As$ at THz frequencies, so we obtain the expression by fitting the data from Ref. [35]. We mainly consider the 6 THz wave generation, where the imaginary parts of the refractive index are 1.17×10^{-2} and 7.545×10^{-2} for revisited AlO_x and $Al_{0.5}Ga_{0.5}As$, respectively. After trying many times, we choose the $W = 4.5$ μm and $H = 2.5$ μm, where $n_p - n_s$ is estimated to be 0.2. At the near-infrared regime, the graphene can be treated as a tunable absorption layer by electrically tuning the Fermi energy level [6,42], and the absorption is very little for our case. We fix $w = 0.8$ μm and $h = 0.4$ μm and try to satisfy the phase-matching condition by changing the Fermi energy level E_F.

Figure 4(a) plots the phase mismatch for THz generation with different frequencies when the pump wavelength is fixed at $\lambda_p = 1.53$ μm. By adjusting E_F and signal wavelength λ_s, the phase-matching condition can be achieved. As shown in Fig. 4(b), when the THz frequency is varied from 4 to 7 THz, the corresponding E_F for phase matching is changed from 0.848 to 2.456 eV and this E_F may be reached through electrical tuning [43]. In detail, the effective refractive index of GSPW and the Fermi energy level for phase-matching at the THz frequency are summarized in Table 1. When the THz frequency decreases, the real part n_i and the loss α_i will increase.

3. RESULTS AND DISCUSSION

A. CW Pump

We first consider the CW pump ($\frac{\partial}{\partial t} = 0$). The coupled-mode equations in Eq. (1) are solved numerically by using the finite difference method [44], and the computational step size is changed step by step to the requirements of higher resolution. For the low loss of the high-index-contrast AlGaAs/AlO_x waveguide and graphene absorption [45], we assume $\alpha_p = \alpha_s = 5$ dB/cm. In the DFG process, the pump and signal wave powers are much higher than the THz wave power. The power-normalized conversion efficiency, which is defined as $\eta = P_i/(P_pP_s)$, are approximately the same for different pump and signal powers. Figure 5(a) shows the power-normalized conversion efficiency as a function of THz wave frequency and waveguide length. From Fig. 5(a), the conversion efficiency increases first and then decreases slightly along the waveguide. This is because the lost THz wave gradually exceeds the generated. With 500 μm waveguide length, the THz wave frequency can range from 5 to 7 THz when the conversion efficiency is larger than 0.5×10^{-6} W^{-1}; the tunable bandwidth can reach 2 THz. The maximum Fermi energy level E_F restricts the high frequency of the THz wave, as shown in Fig. 3(b), and the large loss limits the low frequency and affects the conversion efficiency.

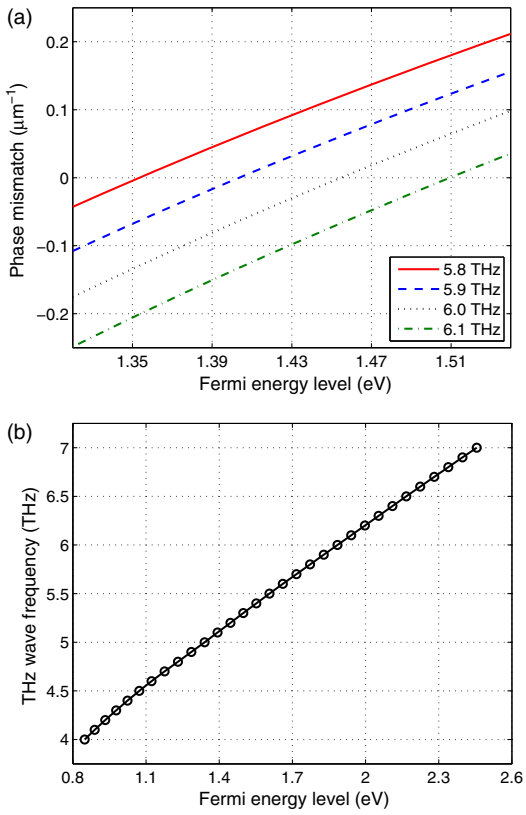

Fig. 4. (a) Phase mismatch Δk as a function of Fermi energy level for 5.8, 5.9, 6.0, and 6.1 THz generation. (b) Phase-matching THz frequency as a function of Fermi energy level.

There are two main mechanisms to suppress the loss. One is enhancing the carrier mobility μ of graphene [22]. The carrier mobility ranges from 8,000 cm^2/(V · s) in mechanical cleavage of bulk graphite [46] to 230,000 cm^2/(V · s) in high-quality suspended graphene [47]. We use moderate carrier mobility $\mu = 10,000$ cm^2/(V · s) in our model. The other one is enlarging the dimension of the waveguide. If width W and height H are of the order of tens of microns, the loss will very small, but meanwhile mode field overlap will be reduced (larger effective nonlinear interaction area A_{eff}).

In order to improve THz wave power, the CW pump and signal powers need to be enhanced, which is difficult to achieve in applications. Compared to the CW pump, it is easier to realize high peak power by a pulse pump, which has the requirement

Table 1. Effective Refractive Index and Fermi Energy Level E_F for Phase-Matching THz Frequency

Wave Frequency/THz	4	4.5	5	5.5	6	6.5	7
E_F/eV	0.848	1.072	1.340	1.606	1.885	2.167	2.456
Effective index	12.171-0.658i	11.223-0.399i	10.477-0.270i	9.890-0.151i	9.357-0.144i	8.927-0.109i	8.552-0.086i

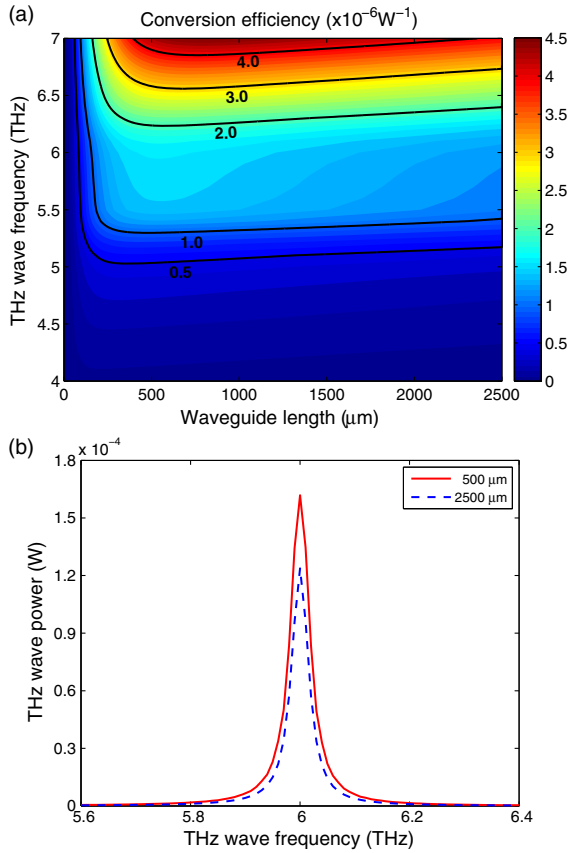

Fig. 5. (a) Contour image of power-normalized conversion efficiency versus waveguide length for different THz wave frequencies. (b) THz wave power versus THz frequency for waveguide length 500 μm and 2500 μm with $P_p = 100$ W and $P_s = 1$ W.

for the full width at half-maximum (FWHM) of conversion efficiency. Figure 5(b) illustrates the THz wave power for different THz frequencies. The power-normalized conversion efficiency is $\eta = 1.619 \times 10^{-6}$ W^{-1} for 6 THz and the FWHM is about 0.044 THz in 500 μm long waveguide.

B. Pulse Pump

The pulse width of the transform-limited Gaussian pulse is about 10 ps for 0.044 THz FWHM with 1.53 μm central wavelength. We use the Gauss pulse pump, and its pulse width is 30 ps. The coupled-mode equations in Eq. (1) are numerically simulated under the walk-off effect, which arises from the very large group index difference between the pump, signal, and THz waves. Figures 6(a)–6(c) display the pulse evolutions for the pump, signal, and THz waves propagating along the waveguide. As shown in Fig. 6(b), the CW signal gradually evolves into a pulsed wave, owing to the DFG process. Figure 6(c) depicts the THz wave evolution, where the peak

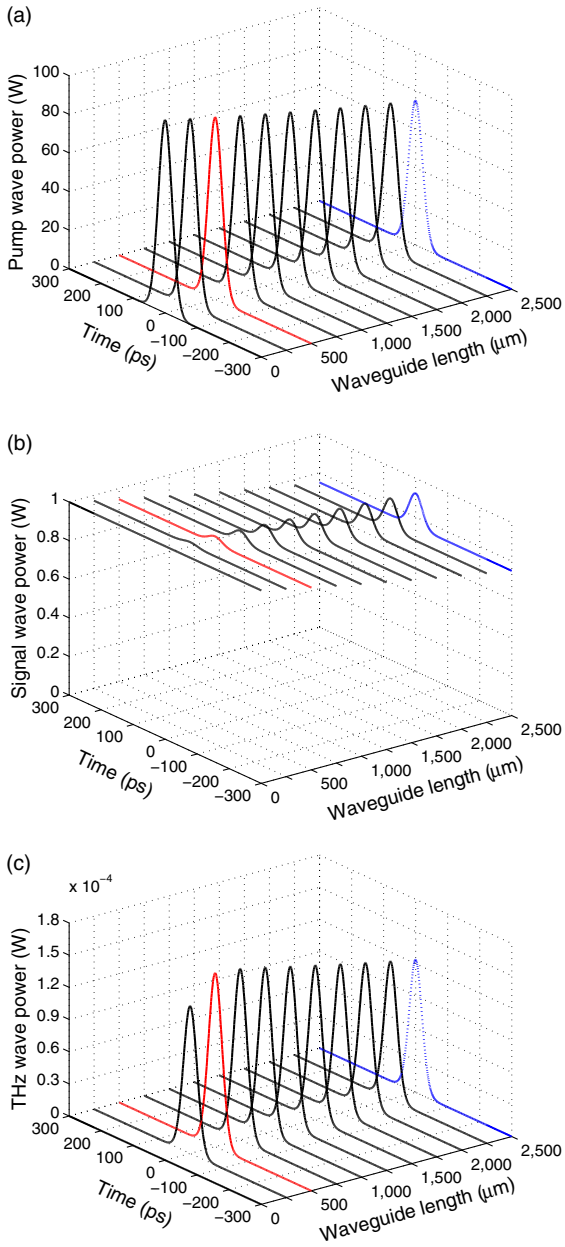

Fig. 6. Optical pulse evolutions along the waveguide with 30 ps pulse input pump with peak power 100 W and 1 W CW input signal: (a) pump wave power, (b) signal wave power, and (c) THz wave power.

power rises to a maximum at 500 μm and then drops slowly. Owing to the short propagation distance, the influence of temporal walk-off between the pump, signal, and THz pulses on the peak power of the THz wave is negligible. Therefore, the power-normalized conversion efficiency of the peak power for

the pulse pump is basically the same as the one for the CW pump, as shown in Fig. 5(a).

4. CONCLUSION

In conclusion, we have investigated in detail a graphene/AlGaAs surface plasmon waveguide for a tunable THz source under near-infrared pumps. To realize the good mode field overlap and phase-matching condition, a hybrid high-index-contrast AlGaAs/AlO_x and graphene surface plasmon waveguide structure is proposed. The GSPW provides deep-subwavelength confinement and single-mode operation at THz frequencies; the birefringent AlGaAs/AlO_x can be used to satisfy the phase-matching condition. Owing to the adjustability of the Fermi energy level in graphene, the waveguide can bring about phase-matching THz generation from 4 to 7 THz when the Fermi energy level of graphene is varied from 0.848 to 2.456 eV. Based on the coupled-mode equations, we numerically calculate the DFG process under CW and pulse pumps. Simulation results show that tunable bandwidth can reach 2 THz with considerable power-normalized conversion efficiency. We note that the GSPW provides a new tunable THz source with flexible dimension, which may benefit the integrated application of optical devices.

Funding. National Natural Science Foundation of China (NSFC) (11547187, 11405073, 61405073); Shandong Provincial Key R&D Program (2017CXGC0416).

REFERENCES

1. K. S. Novoselov, V. I. Fal'Ko, L. Colombo, P. R. Gellert, M. G. Schwab, and K. Kim, "A roadmap for graphene," Nature **490**, 192–200 (2012).
2. Z. Sun, T. Hasan, F. Torrisi, D. Popa, G. Privitera, F. Wang, F. Bonaccorso, D. M. Basko, and A. C. Ferrari, "Graphene mode-locked ultrafast laser," ACS Nano **4**, 803–810 (2010).
3. S. Liu, Z. Li, Y. Ge, H. Wang, R. Yue, X. Jiang, J. Li, Q. Wen, and H. Zhang, "Graphene/phosphorene nano-heterojunction: facile synthesis, nonlinear optics, and ultrafast photonics applications with enhanced performance," Photon. Res. **5**, 662–668 (2017).
4. Q. Bao, H. Zhang, B. Wang, Z. Ni, C. H. Y. X. Lim, Y. Wang, D. Y. Tang, and K. P. Loh, "Broadband graphene polarizer," Nat. Photonics **5**, 411–415 (2011).
5. Y. Wu, B. C. Yao, A. Q. Zhang, X. L. Cao, Z. G. Wang, Y. J. Rao, Y. Gong, W. Zhang, Y. F. Chen, and K. S. Chiang, "Graphene-based D-shaped fiber multicore mode interferometer for chemical gas sensing," Opt. Lett. **39**, 6030–6033 (2014).
6. M. Liu, X. Yin, and X. Zhang, "Double-layer graphene optical modulator," Nano Lett. **12**, 1482–1485 (2012).
7. L. Luo, K. Wang, C. Ge, K. Guo, F. Shen, Z. Yin, and Z. Guo, "Actively controllable terahertz switches with graphene-based nongroove gratings," Photon. Res. **5**, 604–611 (2017).
8. T. Mueller, F. Xia, and P. Avouris, "Graphene photodetectors for high-speed optical communications," Nat. Photonics **4**, 297–301 (2010).
9. H. Zhou, T. Gu, J. F. Mcmillan, N. Petrone, A. V. D. Zande, J. C. Hone, M. Yu, G. Lo, D. L. Kwong, and G. Feng, "Enhanced four-wave mixing in graphene-silicon slow-light photonic crystal waveguides," Appl. Phys. Lett. **105**, 091111 (2014).
10. L. Ren, Q. Zhang, J. Yao, Z. Sun, R. Kaneko, Z. Yan, S. Nanot, Z. Jin, I. Kawayama, and M. Tonouchi, "Terahertz and infrared spectroscopy of gated large-area graphene," Nano Lett. **12**, 3711–3715 (2012).
11. A. N. Grigorenko, M. Polini, and K. S. Novoselov, "Graphene plasmonics," Nat. Photonics **6**, 749–758 (2012).
12. H. Lu, X. Gan, D. Mao, and J. Zhao, "Graphene-supported manipulation of surface plasmon polaritons in metallic nanowaveguides," Photon. Res. **5**, 162–167 (2017).
13. M. Jablan, M. Soljačić, and H. Buljan, "Plasmons in graphene: fundamental properties and potential applications," Proc. IEEE **101**, 1689–1704 (2013).
14. A. Vakil and N. Engheta, "Transformation optics using graphene," Science **332**, 1291–1294 (2011).
15. C. Zhao, D. Mao, J. Zhao, L. Han, L. Fang, X. Gan, and Y. Wang, "Graphene-assisted all-fiber phase shifter and switching," Optica **2**, 468–471 (2015).
16. F. Xie, H. J. Li, J. P. Liu, L. L. Wang, S. X. Xia, X. Zhai, X. Luo, and X. J. Shang, "Graphene-based long-range SPP hybrid waveguide with ultra-long propagation length in mid-infrared range," Opt. Express **24**, 5376–5386 (2016).
17. L. Ju, B. Geng, J. Horng, C. Girit, M. Martin, Z. Hao, H. A. Bechtel, X. Liang, A. Zettl, and Y. R. Shen, "Graphene plasmonics for tunable terahertz metamaterials," Nat. Nanotechnol. **6**, 630–634 (2011).
18. C. H. Gan, "Analysis of surface plasmon excitation at terahertz frequencies with highly doped graphene sheets via attenuated total reflection," Appl. Phys. Lett. **101**, 111609 (2012).
19. T. J. Constant, S. M. Hornett, D. E. Chang, and E. Hendry, "All-optical generation of surface plasmons in graphene," Nat. Phys. **12**, 124–127 (2016).
20. X. He and S. Kim, "Graphene-supported tunable waveguide structure in the terahertz regime," J. Opt. Soc. Am. B **30**, 2461–2468 (2013).
21. X. Zhou, T. Zhang, L. Chen, W. Hong, and X. Li, "A graphene-based hybrid plasmonic waveguide with ultra-deep subwavelength confinement," J. Lightwave Technol. **32**, 4199–4203 (2014).
22. W. Xu, Z. H. Zhu, K. Liu, J. F. Zhang, X. D. Yuan, Q. S. Lu, and S. Q. Qin, "Dielectric loaded graphene plasmon waveguide," Opt. Express **23**, 5147–5153 (2015).
23. M. Tonouchi, "Cutting-edge terahertz technology," Nat. Photonics **1**, 97–105 (2007).
24. A. Barh, B. M. A. Rahman, B. P. Pal, G. P. Agrawal, and R. K. Varshney, "Plastic fiber design for THz generation through wavelength translation," Opt. Lett. **40**, 2107–2110 (2015).
25. Y. Sun, G. Qiao, and G. Sun, "Direct generation of graphene plasmonic polaritons at THz frequencies via four wave mixing in the hybrid graphene sheets waveguides," Opt. Express **22**, 27880–27891 (2014).
26. Y. Takushima, S. Shin, and Y. C. Chung, "Design of a $LiNbO_3$ ribbon waveguide for efficient difference-frequency generation of terahertz wave in the collinear configuration," Opt. Express **15**, 14783–14792 (2007).
27. Y. Huang, T. Wang, Y. Lin, C. Lee, M. Chuang, Y. Lin, and F. Lin, "Forward and backward THz-wave difference frequency generations from a rectangular nonlinear waveguide," Opt. Express **19**, 24577–24582 (2011).
28. Y. H. Avetisyan, "Terahertz-wave surface-emitted difference-frequency generation without quasi-phase-matching technique," Opt. Lett. **35**, 2508–2510 (2010).
29. C. M. Staus, T. F. Kuech, and L. McCaughan, "$AlxGa_{1-x}As$ nested waveguide heterostructures for continuously phase-matched terahertz difference frequency generation," Opt. Express **18**, 2332–2338 (2010).
30. T. Chen, J. Sun, L. Li, and J. Tang, "Proposal for efficient terahertz-wave difference frequency generation in an AlGaAs photonic crystal waveguide," J. Lightwave Technol. **30**, 2156–2162 (2012).
31. Z. Ruan, G. Veronis, K. L. Vodopyanov, M. M. Fejer, and S. Fan, "Enhancement of optics-to-THz conversion efficiency by metallic slot waveguides," Opt. Express **17**, 13502–13515 (2009).
32. Y. Ge, J. Cao, Z. Shen, Y. Zheng, X. Chen, and W. Wan, "Terahertz wave generation by plasmonic-enhanced difference-frequency generation," J. Opt. Soc. Am. B **31**, 1533–1538 (2014).
33. S. Rao, K. Moutzouris, M. Ebrahimzadeh, A. De Rossi, G. Gintz, M. Calligaro, V. Ortiz, and V. Berger, "Influence of scattering and two-photon absorption on the optical loss in GaAs–A_2O_3 nonlinear waveguides measured using femtosecond pulses," IEEE J. Quantum. Electron. **39**, 478–486 (2003).
34. J. Ota, W. Narita, I. Ohta, T. Matsushita, and T. Kondo, "Fabrication of periodically-inverted AlGaAs waveguides for quasi-phase-matched

wavelength conversion at 1.55 μm," Jpn. J. Appl. Phys. **48**, 04C110 (2009).
35. E. D. Palik, *Handbook of Optical Constants of Solids* (Academic, 1985).
36. M. Pu, L. Ottaviano, E. Semenova, and K. Yvind, "Efficient frequency comb generation in AlGaAs-on-insulator," Optica **3**, 823–826 (2016).
37. T. W. Kim, T. Matsushita, and T. Kondo, "Phase-matched second-harmonic generation in thin rectangular high-index-contrast AlGaAs waveguides," Appl. Phys. Express **4**, 082201 (2011).
38. Z. Fei, M. D. Goldflam, J. S. Wu, S. Dai, M. Wagner, A. S. Mcleod, M. K. Liu, K. W. Post, S. Zhu, and G. C. A. M. Janssen, "Edge and surface plasmons in graphene nanoribbons," Nano Lett. **15**, 8271–8276 (2015).
39. C. T. Phare, Y. H. D. Lee, J. Cardenas, and M. Lipson, "Graphene electro-optic modulator with 30 GHz bandwidth," Nat. Photonics **9**, 511–514 (2015).
40. J. Wang, J. Sun, and Q. Sun, "Proposal for all-optical format conversion based on a periodically poled lithium niobate loop mirror," Opt. Lett. **32**, 1477–1479 (2007).
41. P. Y. Chen and A. Alù, "Atomically thin surface cloak using graphene monolayers," ACS Nano **5**, 5855–5863 (2011).
42. M. Liu, X. Yin, E. Ulin-Avila, B. Geng, T. Zentgraf, L. Ju, F. Wang, and X. Zhang, "A graphene-based broadband optical modulator," Nature **474**, 64–67 (2011).
43. F. H. L. Koppens, D. E. Chang, and F. J. G. D. Abajo, "Graphene plasmonics: a platform for strong light-matter interactions," Nano Lett. **11**, 3370–3377 (2011).
44. G. Agrawal, *Nonlinear Fiber Optics*, 4th ed. (Academic, 2007).
45. L. Ottaviano, M. Pu, E. Semenova, and K. Yvind, "Low-loss high-confinement waveguides and microring resonators in AlGaAs-on-insulator," Opt. Lett. **41**, 3996–3999 (2016).
46. Z. Fei, A. S. Rodin, G. O. Andreev, W. Bao, A. S. Mcleod, M. Wagner, L. M. Zhang, Z. Zhao, M. Thiemens, and G. Dominguez, "Gate-tuning of graphene plasmons revealed by infrared nano-imaging," Nature **487**, 82–85 (2012).
47. K. Bolotin, K. Sikes, Z. Jiang, M. Klima, G. Fudenberg, J. Hone, P. Kim, and H. Stormer, "Ultrahigh electron mobility in suspended graphene," Solid State Commun. **146**, 351–355 (2008).